





Quasars as standard candles

IV. Analysis of the X-ray and UV indicators of the disc-corona relation

Matilde Signorini^{1,2,3} , Guido Risaliti^{1,2}, Elisabeta Lusso^{1,2}, Emanuele Nardini² , Giada Bargiacchi^{4,5},
Andrea Sacchi⁶ , and Bartolomeo Trefoloni^{1,2} 

¹ Dipartimento di Fisica e Astronomia, Università di Firenze, Via G. Sansone 1, 50019 Sesto Fiorentino, Firenze, Italy
e-mail: matilde.signorini@unifi.it

² INAF – Osservatorio Astrofisico di Arcetri, Largo Enrico Fermi 5, 50125 Firenze, Italy

³ University of California-Los Angeles, Department of Physics and Astronomy, PAB, 430 Portola Plaza, Box 951547, Los Angeles, CA 90095-1547, USA

⁴ Scuola Superiore Meridionale, Largo S. Marcellino 10, 80138 Napoli, Italy

⁵ Istituto Nazionale di Fisica Nucleare (INFN), Sez. di Napoli, Complesso Univ. Monte S. Angelo, Via Cinthia 9, 80126 Napoli, Italy

⁶ Center for Astrophysics, Harvard & Smithsonian, 60 Garden Street, Cambridge, MA 02138, USA

Received 8 February 2023 / Accepted 19 June 2023

ABSTRACT

Context. A non-linear relation between quasar monochromatic luminosities at 2500 Å and 2 keV holds at all observed redshifts and luminosities, and it has been used to derive quasar distances and to build a Hubble diagram of quasars. The choice of the X-ray and UV indicators has so far been somewhat arbitrary and has typically relied on photometric data.

Aims. We aim to determine the X-ray and UV proxies that provide the smallest dispersion of the relation in order to obtain more precise distance estimates and to confirm the reliability of the X-ray-to-UV relation as a distance indicator.

Methods. We performed a complete UV spectroscopic analysis of a sample of ~1800 quasars with SDSS optical spectra and *XMM-Newton* X-ray serendipitous observations. In the X-rays, we analysed the spectra of all the sample objects at redshift $z > 1.9$, while we relied on photometric measurements at lower redshifts. As done in previous studies, we analysed the relation in small redshift bins, using fluxes instead of luminosities.

Results. We show that the monochromatic fluxes at 1 keV and 2500 Å are, respectively, the best X-ray and UV continuum indicators among those that are typically available. We also find a tight relation between soft X-ray and Mg II $\lambda 2800$ Å line fluxes, and a marginal dependence of the X-ray-to-UV relation on the width of the Mg II line.

Conclusions. Our analysis suggests that the physical quantities that are more tightly linked to one another are the soft X-ray flux at ~1 keV and the ionising UV flux blueward of the Lyman limit. However, the ‘usual’ monochromatic fluxes at 2 keV and 2500 Å estimated from photometric data provide an almost as tight X-ray-to-UV relation, and can be used to derive quasar distances. The Hubble diagram obtained using spectroscopic indicators is fully consistent with the one presented in previous papers, based on photometric data.

Key words. galaxies: active – quasars: general – quasars: supermassive black holes – methods: statistical

1. Introduction

Quasars are the most luminous persistent objects in our Universe. Their spectral energy distribution (SED) is complex; it goes from the radio to the X-rays, with the most intense emission emerging at optical–UV wavelengths (e.g., [Sanders et al. 1989](#); [Richards et al. 2006](#); [Elvis et al. 2012](#)). The origin of this emission is attributed to accretion from an optically thick and geometrically thin disc around the central supermassive black hole (SMBH; [Shakura & Sunyaev 1973](#)). For decades, the presence of a non-linear relation between the X-ray and UV luminosities of quasars has been observed ([Tananbaum et al. 1979](#)). This relation is usually parameterised as $\log(L_X) = \gamma \log(L_{UV}) + \beta$, where the slope is found to be $\gamma \simeq 0.6$ over a wide range of redshifts and luminosities (e.g., [Steffen et al. 2006](#); [Lusso et al. 2010](#); [Young et al. 2010](#)). This relation must be based on the interaction between the accretion disc, which emits mainly in the UV, and the so-called X-ray corona, which consists of a hot-electron plasma. UV photons coming from the disc are up-scattered in

the corona, where they reach X-ray energies. It is clear that such an inverse-Compton mechanism can rapidly cool down the electron plasma, thus halting the production of X-rays. Since the X-ray emission of quasars is, instead, found to be persistent, a mechanism that refuels the corona with energy must exist. Given that the engine of a quasar is the infall of matter into the central SMBH through the accretion disc, this is also where the energy that refuels the X-ray corona most likely comes from. The existence of the L_X – L_{UV} relation is therefore thought to be linked to such a mechanism, even if the exact physical process is still not completely understood. Modelling attempts have considered the reprocessing of the radiation from a non-thermal electron–positron pair cascade ([Svensson 1982](#)), buoyancy, and the reconnection of magnetic fields as a way to dissipate the gravitational power ([Haardt & Maraschi 1991, 1993](#); [Svensson & Zdziarski 1994](#)) or the presence of a viscosity-heated corona in which friction produces the heating ([Meyer et al. 2000](#)).

In addition to its relevance to quasar physics, the non-linearity of the X-ray-to-UV luminosity relation and the

non-variability of its parameters make it possible to determine the luminosity distance of quasars, and therefore to use them as standard candles. This cosmological implication has been evident since the discovery of the L_X-L_{UV} relation. However, its application was hindered by the very high observed dispersion (~ 0.4 dex), which made the luminosity distance estimates too uncertain to be useful for cosmology. In recent years, it has been shown that most of this dispersion is due to observational issues, which can largely be removed by neglecting quasars that are affected by dust reddening, gas absorption, or Eddington bias from the sample (i.e., [Lusso & Risaliti 2016](#); [Lusso et al. 2020](#)). This way, the observed dispersion is significantly reduced to $\sim 0.20-0.25$ dex. The resort to quasars as standard candles allows us to extend the Hubble diagram up to redshift values much higher than the ones that are achieved with supernovae Ia ([Scolnic et al. 2018, 2022](#)). This extended Hubble diagram is in agreement with the predictions of a flat Λ CDM cosmology up to a redshift of $z \sim 1.5$. At the same time, it shows a 4σ tension with the concordance model at higher redshifts (e.g., [Risaliti & Lusso 2019](#); [Bargiacchi et al. 2021, 2022](#)). Given the obvious relevance of these cosmological results and the absence of a physical model explaining the X-ray-to-UV luminosity relation, it is fundamental to validate it observationally, ruling out any possible redshift dependence and systematic biases in the selection of the sample and/or in the flux measurements. A possible way to perform such checks has been proposed by other groups (e.g., [Khadka & Ratra 2021](#)) based on the comparison of the data with several different cosmological models. However, it is impossible to perform a complete observational and cosmology-independent validation of a standard candle beyond the maximum redshift at which it has been validated by other distance indicators. Here, we used a different approach; in order to convince ourselves that the adoption of our method beyond $z = 1.5$ (at lower redshift it has already been validated, by the comparison with SNIa (see, e.g., [Lusso et al. 2020](#)) is well motivated, we want to further exploit our observational data set, in particular using the spectroscopic data instead of just the photometric ones, for a better analysis of the X-ray-to-UV relation. In this paper, we focus on the search of the optimal X-ray and UV indicators for the observed relation. In subsequent works, we will focus on the analysis of the intrinsic dispersion of the relation (Signorini et al., in prep.), and on the analysis of the average spectral properties of our sample as a function of redshift (Trefoloni et al., in prep.).

In previous studies, the 2500-Å and 2-keV luminosities have been used as L_{UV} and L_X , respectively. The reasons behind this choice are mainly historical. Although the exact nature of the physical interaction between the disc and the corona is not completely understood, it seems unlikely to involve two monochromatic luminosities. Conversely, it is reasonable to believe that it should depend on the UV and X-ray emission over wider bands. Indeed, by adopting monochromatic luminosities for L_X and L_{UV} to analyse the L_X-L_{UV} relation, we are simply choosing two proxies of the overall emission. Therefore, we can ask ourselves which quantities work better to minimise the observed dispersion of the relation. The main aim of this paper is to discuss the choice of the L_X and L_{UV} indicators to establish whether it is possible to further reduce the observed dispersion, and so gain a better understanding of the physics behind the L_X-L_{UV} relation.

We also note that in most of our previous studies, the UV monochromatic luminosities have always been derived from photometric data. In principle, deriving luminosities from a spectroscopic analysis is a more precise method. This is true especially in the UV, as a complete spectral fitting allows us to

accurately take into account all the emission lines, while in photometric estimates some contamination from line emission that is not separated from the continuum might remain. It is then worth investigating the results of implementing UV measurements derived from a thorough spectroscopic analysis instead of the photometric ones.

The paper is structured as follows. In Sect. 2, we present the data sample and the products of our spectroscopic analysis. In Sect. 3, we make use of the spectroscopic sample to investigate the X-ray-to-UV relation using different proxies of the UV and X-ray fluxes. In Sect. 4, we discuss the Mg II line width as a possible additional parameter of the relation. Section 5 presents the discussion of our results, consisting of two parts: (a) the analysis of the differences among the parameter values of the relation depending on the choice of the UV and/or X-ray proxies; and (b) the implications for the use of quasars as cosmological distance estimators. Our conclusions are summarised in Sect. 6. Source luminosities were estimated by adopting a concordance flat Λ CDM cosmology with $H_0 = 70 \text{ km s}^{-1} \text{ Mpc}^{-1}$ and $\Omega_M = 0.3$.

2. Data

Our sample consists of 1764 quasars, all of which have available UV and X-ray data in public catalogues and are included in the sample published by [Lusso et al. \(2020\)](#). In particular, we considered in said sample all the sources with available X-ray observations from the *XMM-Newton* satellite. More in detail, the sample is made of the following subsamples of the [Lusso et al. \(2020\)](#) one: SDSS-4XMM (1644 objects), *XMM-Newton* $z \simeq 3$ (14 objects), and XXL (106 objects). Out of 1764, 772 objects have spectra obtained with the BOSS spectrograph, while the remaining ones have spectra acquired with the original SDSS one. As discussed in the next section, our analysis was performed by dividing the sample into small redshift bins. The high-redshift ($z \geq 4$) objects discussed in Sects. 2.5 and 2.6 of [Lusso et al. \(2020\)](#) are too sparse in redshift for the kind of analysis that we are interested in. This is why we excluded them from this analysis even though they have *XMM-Newton* observations available.

Detailed information regarding the sample can be found in [Lusso et al. \(2020, see their Sect. 2\)](#). Here, we briefly recall that the selected objects are all radio-quiet and not flagged as broad absorption line (BAL) quasars. Furthermore, they have blue optical colours and steep X-ray spectra (photon index $\Gamma > 1.7$), and they have deep enough X-ray observations to avoid biases towards brighter-than-average states. These properties make them suitable for a detailed analysis of the X-ray-to-UV relation, taking advantage of the homogeneity of both the source properties and the observational data.

2.1. Optical–UV spectral analysis

We performed the fitting procedure of each of the SDSS spectra using the software package QSFit ([Calderone et al. 2017](#)). The Signal-to-noise ratio (S/N) per pixel for our sample is typically between 8 and 20 (pixels in SDSS/BOSS spectra are logarithmically spaced, with a width of 10^{-4} dex). For each object, we derived the continuum slope and the emission line properties (i.e., integrated line flux, rest-frame equivalent width, full width at half maximum, velocity offset). We also recorded the continuum monochromatic flux at different rest-frame wavelengths (1350 Å, 2500 Å, 3000 Å, 4400 Å, 5100 Å). When one or more of these five rest-frame wavelengths did not fall in the range

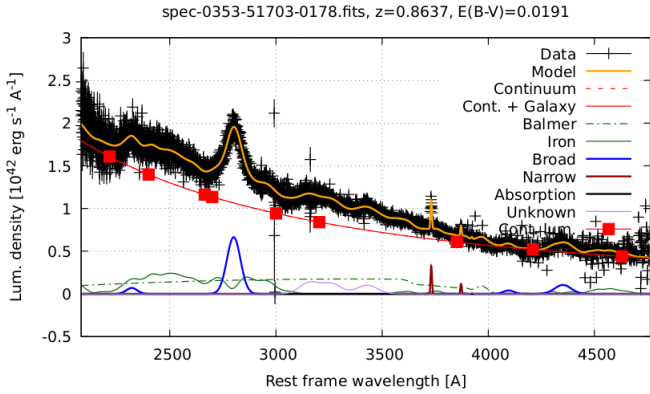


Fig. 1. Example of UV spectrum together with the best fit (yellow line) and the various spectral components. The QSFit code assumes, for calculating luminosities, a standard Λ CDM cosmology with $H_0 = 70 \text{ km s}^{-1} \text{ Mpc}^{-1}$, $\Omega_M = 0.3$, and $\Omega_\Lambda = 0.7$ (Calderone et al. 2017).

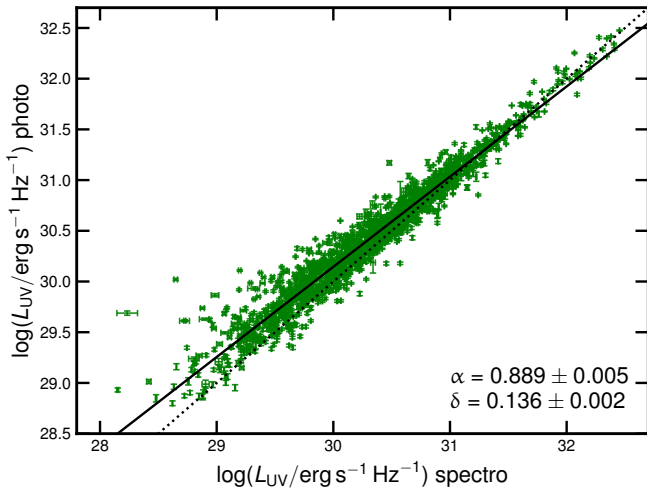


Fig. 2. Relation between monochromatic luminosity at 2500 \AA derived from photometry as a function of the one obtained from the spectral analysis of our sample. The dotted line represents the one-to-one relation. The solid black line is the best-fit regression between these two parameters. The resulting slope and dispersion are reported in the figure.

covered by the SDSS spectrum, the relative monochromatic fluxes were derived through the extrapolation of the best-fit continuum. A typical spectrum with its best-fit model is shown in Fig. 1, while a detailed description of the fitting procedure is provided in Appendix A. We note that the QSFit code returns results in luminosities, and not fluxes, assuming a standard Λ CDM cosmology with $H_0 = 70 \text{ km s}^{-1} \text{ Mpc}^{-1}$, $\Omega_M = 0.3$, and $\Omega_\Lambda = 0.7$. Given that we are interested in flux measurements, we derived them from the obtained luminosities assuming the same cosmology. All the objects also have photometric flux estimates, derived as described in Lusso et al. (2020).

For completeness, Fig. 2 presents the comparison between the monochromatic luminosity at 2500 \AA derived from photometry as a function of the one obtained from the spectral analysis of our sample. The dotted line represents the one-to-one relation, while the solid black line is the best-fit regression between these two parameters. The resulting slope and dispersion are also reported in the figure. Interestingly, the relation between the two monochromatic flux estimates is significantly non-linear. The

discussion of this result is beyond the scope of this paper, and we will address it in a forthcoming work.

2.2. X-ray spectral analysis

Regarding the X-ray data, we performed a complete spectral analysis and derived the photon index Γ and the monochromatic fluxes for all the objects in our sample at a redshift higher than 1.9 (292 out of 1764). This is part of the ongoing effort to achieve better estimates of both the X-ray monochromatic fluxes that are used in the L_X-L_{UV} relation and the X-ray photon indexes Γ , which are key parameters in the sample selection to remove possibly obscured quasars¹. The spectroscopic fluxes for the $z > 1.9$ are fully consistent with the photometric ones. The only improvement we obtained is a slight decrease of the dispersion of the UV-to-X-ray relation (see the discussion in Sacchi et al. 2022). Therefore, we did not extend the (quite time consuming) spectroscopic analysis further. A detailed description of the X-ray spectroscopic analysis can be found in Appendix B.

For the objects at redshift $z < 1.9$, the rest-frame 2-keV flux is computed starting from the observer's frame fluxes at 0.5–2 keV (F_S) and 2–12 keV (F_H) tabulated in the 4XMM-DR9 serendipitous source catalogue. An analysis of simulated power-law spectra with typical *XMM-Newton* responses and effective areas shows that the monochromatic fluxes at 1 keV ($f_{1 \text{ keV}}$) and at 3.45 keV ($f_{3.45 \text{ keV}}$) are ‘pivot points’ for the soft and hard bands, respectively, for example, the relation between these monochromatic fluxes and the total F_S and F_H fluxes is almost insensitive to the photon index Γ . Therefore, we estimated $f_{1 \text{ keV}}$ and $f_{3.45 \text{ keV}}$ from F_S and F_H assuming the same photon index used in the 4XMM catalogue ($\Gamma = 1.42$). We then used the power law defined by these two fluxes to compute both a new photometric photon index and the rest-frame monochromatic fluxes at different energies, as needed for our analysis (see the next sections). More details on this procedure are discussed in Risaliti & Lusso (2019) and Lusso et al. (2020).

3. Analysis of the X-ray-to-UV relation

The first step of our analysis of the X-ray-to-UV relation is a comparison of the results obtained adopting the new spectroscopic fluxes at the traditional reference wavelength of 2500 \AA with those based on our previous UV and X-ray flux values from photometric data. Before showing the results, we outline the fitting method, which will be the same throughout the paper.

As in our previous studies, we always performed our analysis by dividing the sample into a fixed number of redshift bins, such that for each bin, $\Delta \log z < 0.1$. For this sample, we chose 11 bins in the 0.38–3.48 redshift range, with a width of each bin of $\Delta \log z = 0.08$. In doing so, the differences among luminosity distances for the objects in a given bin are negligible compared to the dispersion in the relation. In particular, we checked with simulated data that the best-fit slope is always correctly recovered, provided that $\Delta \log z < 0.1$. The relation can therefore be re-written in terms of fluxes as

$$\log(f_X) = \gamma \log(f_{UV}) + \beta', \quad (1)$$

¹ The spectroscopically derived photon indexes Γ are used to improve our sample selection, adopting the criterion of $\Gamma > 1.7$. This introduces an inhomogeneity in the selection of objects at low and at high redshift. However, we found that the only difference between the photometric and spectroscopic selection at $z > 1.9$ is a slight decrease of the dispersion of the relation in the spectroscopically selected sample, without any systematic effects on the parameters of the relation.

where β' is related to the normalisation β of the L_X-L_{UV} relation through the following expression:

$$\beta'(z) = 2(\gamma - 1) \log D_L(z) + (\gamma - 1) \log 4\pi + \beta. \quad (2)$$

With this choice, we can perform our analysis independently of the cosmological model used to compute the luminosities. This is fundamental as we want our results on the physical relation between UV and X-ray emission not to be biased as a consequence of the adopted cosmology, which is essential to subsequently implementing quasars as cosmological probes. Furthermore, fitting the X-ray-to-UV relation in separate redshift bins allows us to investigate possible trends of its parameters with redshift, which is also crucial for cosmological applications. The parameters derived from the fitting procedure are γ , β' , and the intrinsic dispersion δ . As in our previous works, we introduced the parameter δ because the observational errors on L_X (or f_X) and L_{UV} (or f_{UV}) alone cannot explain the observed scatter of the L_X-L_{UV} (or f_X-f_{UV}) relation. For each bin, we also calculated the total dispersion δ_T , which can be considered to be the square root of the quadratic sum of the total observational error on the fluxes and the intrinsic dispersion δ .

To perform the fit, a Bayesian approach of likelihood maximisation was used: this allowed us to estimate the parameters γ and β' while also taking the presence of the intrinsic dispersion δ into account, by modifying the likelihood function accordingly. Furthermore, using this approach we can obtain reliable estimates of the uncertainties on the parameters. We used the *emcee* code, which is an implementation of Goodman and Weare's Affine Invariant Markov chain Monte Carlo (MCMC) Ensemble sampler (Foreman-Mackey et al. 2013). We performed a fit for each redshift bin, adopting a sigma clipping at 3σ in order to exclude the few strong outliers that might still be present after the quality-selection procedure. The sigma-clipping procedure removes $\sim 1\%$ of the sample, both when photometric and when spectroscopic data are used. The parameters of the relation (γ and β') do not change with the sigma clipping; the only effect is on the dispersion parameter, which decreases by 0.02 dex for both samples.

Once we established that no significant trend of the fitted parameters in the redshift bins was to be found, we derived the average value for the parameters γ , δ , and δ_T by weighing each value for the number of objects in that bin. We remind the reader that β' , instead, is expected to vary with redshift through its dependence on D_L (see Eq. (2)).

Following this procedure, we tested the X-ray-to-UV relation using the 2500 Å monochromatic flux obtained in the spectroscopic analysis, while we keep assuming the photometric 2-keV monochromatic flux as f_X . The slope parameter γ of the flux-based relation is always found to be lower than in our previous analyses, where the photometric flux at 2500 Å was used (Lusso & Risaliti 2016, 2017; Risaliti & Lusso 2019; Lusso et al. 2020), with an average value of $\gamma = 0.46$, as shown in Fig. 3, left panel. The slope does not show a systematic redshift trend. We tested this by fitting the 11 γ values as a function of redshift with a line, $\gamma = mz + q$, finding the best-fit values of the slope and intercept to be $m = -0.02 \pm 0.03$ and $q = 0.49 \pm 0.05$. The slope m is statistically consistent with zero, whilst the intercept q is statistically consistent with the average value of $\langle \gamma \rangle = 0.46$.

The redshift independence of the γ parameter in the X-ray to UV relation has already been thoroughly discussed in previous works, and it is now corroborated by employing spectroscopically derived monochromatic fluxes. Regarding the dispersion

parameter δ , the fact that we obtained a value of 0.22 dex, which is similar to (although slightly larger than) the one found when using photometric fluxes, is by itself an interesting result for our understanding of the physics of the X-ray-to-UV relation. If the 'true' quantity behind the relation were the monochromatic luminosity at 2500 Å, we would expect the intrinsic dispersion to be lower, as a spectroscopic fit more accurately describes the true quasar continuum at a given wavelength when compared to the estimates we obtain from photometry. As this is not the case, it is possible that both spectroscopic and photometric fluxes are simply two different proxies of the quasar UV emission, which are almost equivalently effective in terms of the tightness of the resulting relation.

Starting from these considerations, we expanded our analysis in order to search for the optimal UV and X-ray indicators, under the assumption that both the UV and the X-ray spectra of quasars can be described by a power-law continuum over the range in question. We expect the 'true' physical relation to hold between the emission within a given frequency range in both the UV and the X-rays. For any frequency range, we can determine a characteristic frequency whose monochromatic flux would work as the best proxy according to the following argument. Let us consider a power-law spectrum between the frequencies ν_1 and ν_2 . Then, for a fixed total flux in the (ν_1, ν_2) interval, there will be a frequency, ν_C , which we call 'characteristic', such that the monochromatic flux value f_{ν_C} does not depend on the slope of the power law, as this is the point that divides the spectral range into two intervals with the same weight. In terms of frequency, we see that $\nu_C \approx \sqrt{\nu_1 \nu_2}$. This result is exact only if the spectral index is -1 (i.e., $f_\nu \propto \nu^{-1}$), and the instrumental response in the (ν_1, ν_2) interval is flat. We argue that if we want to use a monochromatic flux as a proxy for the emission over a relatively wide wavelength range, the monochromatic flux at the 'characteristic energy' would be the best choice. Indeed, it would be (nearly) independent of the specific value of the slope of the power-law spectrum and it would be directly related to the global emission in the (ν_1, ν_2) range. This argument works for the choice of both the UV and the X-ray proxies.

To find the characteristic frequency, we considered that any generic frequency ν can be associated with the characteristic one through the following expression:

$$f_\nu = f_{\nu_C} \left(\frac{\nu}{\nu_C} \right)^\Upsilon, \quad (3)$$

where Υ is the slope of the power law, ν_C is the characteristic frequency, and f_{ν_C} is the corresponding flux. If we assume that Eq. (1) holds for the characteristic energy flux f_{ν_C} and we substitute Eq. (3), we see that if we use f_ν , we also expect a correlation with the power-law slope Υ . We expect to find a correlation with Υ when a non-characteristic flux is used, while we expect no correlation with Υ when the flux at the characteristic energy is used. Furthermore, the slope of such a correlation would depend on the ratio between the frequency that we are using and the characteristic frequency. So, we can define a modified version of the flux-flux relation that also takes into account the correlation with the slope Υ :

$$\log(f_X) = \gamma \log(f_{UV}) + \zeta \Upsilon + \beta', \quad (4)$$

where ζ is the slope of such correlation, which we can include in our fitting procedure as an additional parameter by modifying the likelihood function accordingly. We can use this relation to search for the characteristic energy in the UV (and likewise in

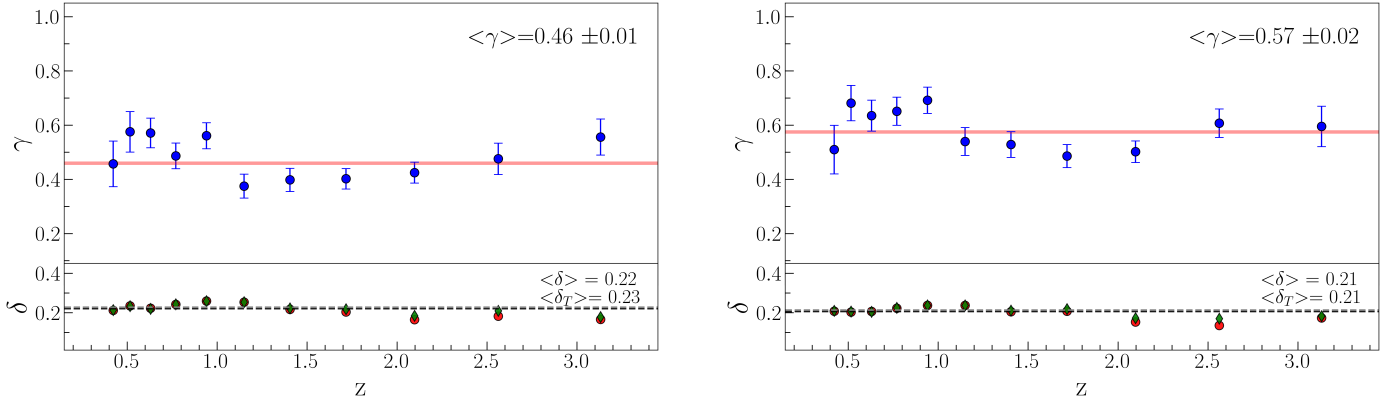


Fig. 3. Slope γ , total dispersion δ_T (as green diamonds), and intrinsic dispersion δ (as red circles) of the X-ray (2 keV) to UV (2500 Å) flux relation in 11 narrow redshift bins. Left panel: results with the UV flux derived from spectroscopic data. Right panel: results with photometric UV fluxes.

Table 1. Results of the search for the UV characteristic energy.

Wavelength	γ	ζ	δ	δ_T
1350 Å	0.43 ± 0.02	0.05 ± 0.02	0.23	0.23
2500 Å	0.45 ± 0.02	0.05 ± 0.02	0.22	0.23
3000 Å	0.45 ± 0.02	0.05 ± 0.02	0.23	0.23
4400 Å	0.41 ± 0.02	0.09 ± 0.02	0.23	0.23
5100 Å	0.39 ± 0.02	0.09 ± 0.02	0.23	0.24

the X-rays) of the $f_X - f_{UV}$ relation. The value of the parameter ζ is indeed related to the characteristic frequency, as

$$\zeta = \gamma \log\left(\frac{\nu_C}{\nu}\right). \quad (5)$$

3.1. UV monochromatic proxy

Based on the aforementioned argument, we tested which monochromatic flux works as the best UV proxy by including the UV continuum slope as an additional parameter to the $L_X - L_{UV}$ relation. As before, the fit was performed in 11 redshift bins and by using fluxes instead of luminosities. We used the same five different monochromatic fluxes derived from the spectroscopic analysis, as discussed in the previous section. We tested relation (4), with the additional parameter ζ to be fitted and the UV slope Υ .

In terms of the parameter γ , we found average values in the range between 0.39 (for the 5100 Å flux) to 0.45 (for the 2500 Å and 3000 Å fluxes). The significance of the additional parameter ζ is found to be very small for all the chosen UV proxies, although a tentative increase is seen at longer wavelengths. The results are summarised in Table 1 and might have different explanations. It could be that a simple power law is not a sufficiently representative model for the optical–UV (1350–5100 Å) continuum, so the ‘characteristic energy argument’ does not completely hold, owing to, for example, some host-galaxy contribution at longer wavelengths. It could also happen that the region of the disc that is truly physically linked to the X-ray corona is emitting at wavelengths shorter than (or across) the UV peak, so the optical–UV continuum slope is not the correct quantity to be taken into account.

Given these results, each of the five proposed optical–UV proxies could, in principle, work equivalently well. The 2500 Å

wavelength falls within the SDSS spectra for the widest possible redshift range in our sample. This means that there are relatively few objects for which the monochromatic flux is derived through extrapolation, which might be less reliable than the directly measured ones. Indeed, the 2500 Å flux provides the lowest dispersion, although marginally. We can thus consider this flux as the best proxy available.

We conclude this analysis with an additional fit required to compare the results obtained here to those published in previous papers on the X-ray-to-UV relation in quasars. Throughout this paper, we use quantities derived from the spectroscopic analysis as f_{UV} for the first time. However, in all our previous works the UV monochromatic flux has been derived from the SDSS photometric data through an interpolation procedure (Lusso et al. 2020). We refer to this latter quantity as the ‘photometric’ UV flux. In order to facilitate comparison, we fitted the relation between fluxes with the 2-keV monochromatic flux as f_X and the photometric flux at 2500 Å as f_{UV} within the same redshift range of 0.38–3.48 and over 11 redshift bins. We obtain a mean value of the slope of $\gamma = 0.57 \pm 0.02$ and an intrinsic dispersion of $\delta = 0.21$ dex. The results are shown in Fig. 3 in the right panel.

3.2. X-ray proxy

The X-ray spectrum of quasars can also be described by a power law. Therefore, analogous arguments regarding the choice of the ‘characteristic energy’ can be made, and we can investigate whether the 2-keV monochromatic luminosity is the best choice for L_X . The argument is the same as that described in the previous section; if we are not using the characteristic flux as f_X , we expect a dependence on the X-ray continuum slope, which in this case is described by the photon index Γ :

$$f_{2\text{keV}} = f_{Ec} \left(\frac{E_{2\text{keV}}}{E_C} \right)^{1-\Gamma}. \quad (6)$$

We note that the X-ray spectral shape is much better described by a simple power law than the UV one, as there are no other prominent spectral features. Therefore, the determination of the ‘characteristic energy’ may be more straightforward than for the UV range. The main difference with the previous section is that for the X-ray data, we still do not have a complete spectral analysis for each object, so we rely on photometrically derived estimates of both the monochromatic flux and the photon index for most of them.

We tested whether any dependence on the photon index Γ is found when using the 2-keV monochromatic flux, implementing a modified version of Eq. (4) in our fitting procedure:

$$\log(f_X) = (\Gamma - 1)\xi + \gamma \log(f_{UV}) + \beta', \quad (7)$$

where

$$\xi = \log\left(\frac{E_C}{E}\right). \quad (8)$$

We performed the analysis using the spectroscopically derived flux at 2500 Å as f_{UV} . As before, we used 11 redshift bins, in the redshift range of $z = 0.38$ – 3.48 . We obtain a mean value of the slope of $\gamma = 0.47 \pm 0.02$, which is perfectly consistent with the previous values, and a significant f_X – Γ correlation parameter, with a mean value among the redshift bins of $\xi = -0.31 \pm 0.02$. The mean value of the intrinsic dispersion parameter becomes lower, with $\delta = 0.19$ dex instead of 0.22 dex.

The value of the parameter ξ allows us to determine where the X-ray characteristic energy is located according to Eq. (8). Given the obtained value $\xi = -0.31$, we infer that the characteristic energy should be located at ~ 1 keV. The characteristic energy depends on the physical extent of the X-ray power law, which is not well known. Considering the minimum and the maximum energy of the (unknown) optimal X-ray range for the relation, so that the characteristic energy $E_C \sim \sqrt{E_{\min} E_{\max}}$, our estimate of $E_C \sim 1$ keV, might mean, for example, $E_{\min} \sim 0.01$ keV and $E_{\max} \sim 100$ keV, or $E_{\min} \sim 0.1$ keV and $E_{\max} \sim 10$ keV. Employing both the 2-keV flux and the parameter Γ in the relation mimics the employment of the 1-keV flux, which is almost insensitive to the exact value of Γ .

In order to test our assumption that the 1-keV energy is the X-ray characteristic energy, we derived, from photometric data, the monochromatic flux at 1 keV for all the sources in our sample; for objects at a redshift higher than 1.9, we derived it from the fit of the X-ray spectrum. We then performed the aforementioned analysis again. We found no significant correlation with the photon index Γ , with values of ξ consistent with zero. This confirms that we have found the true characteristic energy. Furthermore, by adopting the combination of the 1-keV flux as f_X and the 2500 Å spectroscopic flux as f_{UV} , we obtain a mean slope value of $\gamma = 0.46 \pm 0.01$ (consistent with the previous estimate), a value of ξ consistent with zero, and consistent values of the intrinsic and total dispersion parameters, with $\delta = 0.18$ dex and $\delta_T = 0.21$ dex.

We recall that allowing for an intrinsic dispersion parameter δ is necessary because the scatter of the observational points in the f_X – f_{UV} relation cannot be entirely justified by the errors on the observed fluxes. Given that the rest-frame 1-keV emission is not between the two X-ray pivot points (see Sect. 2.2), and that with increasing redshift it gets progressively farther away from the observed energy range, the 1-keV fluxes are less precisely measured, with a mean observational error higher than the one obtained for the 2-keV monochromatic fluxes' estimates. Consequently, it is possible that part of the observed decrease of the intrinsic dispersion with the 1-keV flux as f_X is due to an increase of the mean observational error on the 1-keV fluxes. However, when adopting the 1-keV flux instead of the 2-keV one, we also notice a reduction of the total dispersion δ_T . We thus conclude that, although the 1-keV flux is a less precise proxy in terms of its associated observational error, it can still be stated that, physically, it is a more accurate one.

To sum up, in this section we discuss the choice of the UV and X-ray proxies of the L_X – L_{UV} relation. We argue that the

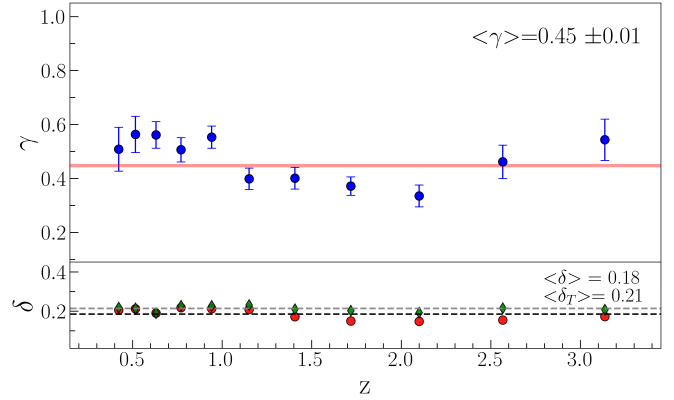


Fig. 4. Slope parameter γ as function of redshift, as obtained by fitting Eq. (1) when the monochromatic flux at 2500 Å derived from the spectroscopic analysis is used as f_{UV} and the monochromatic flux at 1 keV is used as f_X . The mean value of γ is 0.45 ± 0.01 , and we can see that there is no clear trend with redshift.

best choice is, in both cases, in the monochromatic flux whose frequency acts as the characteristic energy of the spectral emission. Regarding the UV side of the relation, we found no clear trend as a function of the continuum slope, and therefore it can be stated that the monochromatic flux at 2500 Å is a good choice, as it provides the smallest intrinsic dispersion and it can be directly observed in optical–UV spectra for a wide redshift range. Regarding the X-ray side of the relation, we found a significant correlation with the photon index Γ when the 2-keV flux is used as f_X . The observed dispersion decreases when the latter dependence is taken into account. From this, we can deduce that the X-ray characteristic energy should fall around 1 keV. The adoption of the 1-keV flux, indeed, results in no correlation with the photon index Γ , and a lower dispersion too. However, the photometric estimates of the 1-keV fluxes are significantly less precise than the ones at 2 keV for our sample.

In Fig. 4, we show the results in terms of the parameter γ as a function of redshift, with the (spectroscopic) 2500 Å monochromatic flux as f_{UV} and the monochromatic flux at 1 keV as f_X . In Fig. 5, we also show the f_X – f_{UV} relation in the 11 redshift bins. With these choices, both the intrinsic and the total dispersion of the relation between fluxes are reduced. We checked again for the redshift dependence of the slope parameter γ , again by fitting the 11 values with a line as a function of redshift. We found the best-fit slope to be $m = -0.04 \pm 0.03$. Such a value is compatible with zero at 1.3σ and, overall, very small. We stress again that the non-dependence of the γ parameter with redshift is fundamental to showing that (i) the physical mechanism behind the relation is the same at all the observed redshifts, and (ii) we can safely use quasars as standard(isable) candles for cosmology.

3.3. Mg II line flux as UV proxy

The fluxes of quasar recombination lines depend on the intensity of the photoionising continuum. As such, these fluxes could constitute good indicators of the disc primary emission. We chose to test this hypothesis by analysing the f_X – f_{UV} relation using the 1-keV monochromatic flux as f_X and the flux of the Mg II $\lambda 2800$ Å emission line as f_{UV} .

The Mg II $\lambda 2800$ Å resonant line (Netzer 1980; Krolik & Kallman 1988) requires the second ionisation of magnesium by photons with energies exceeding 15.035 eV,

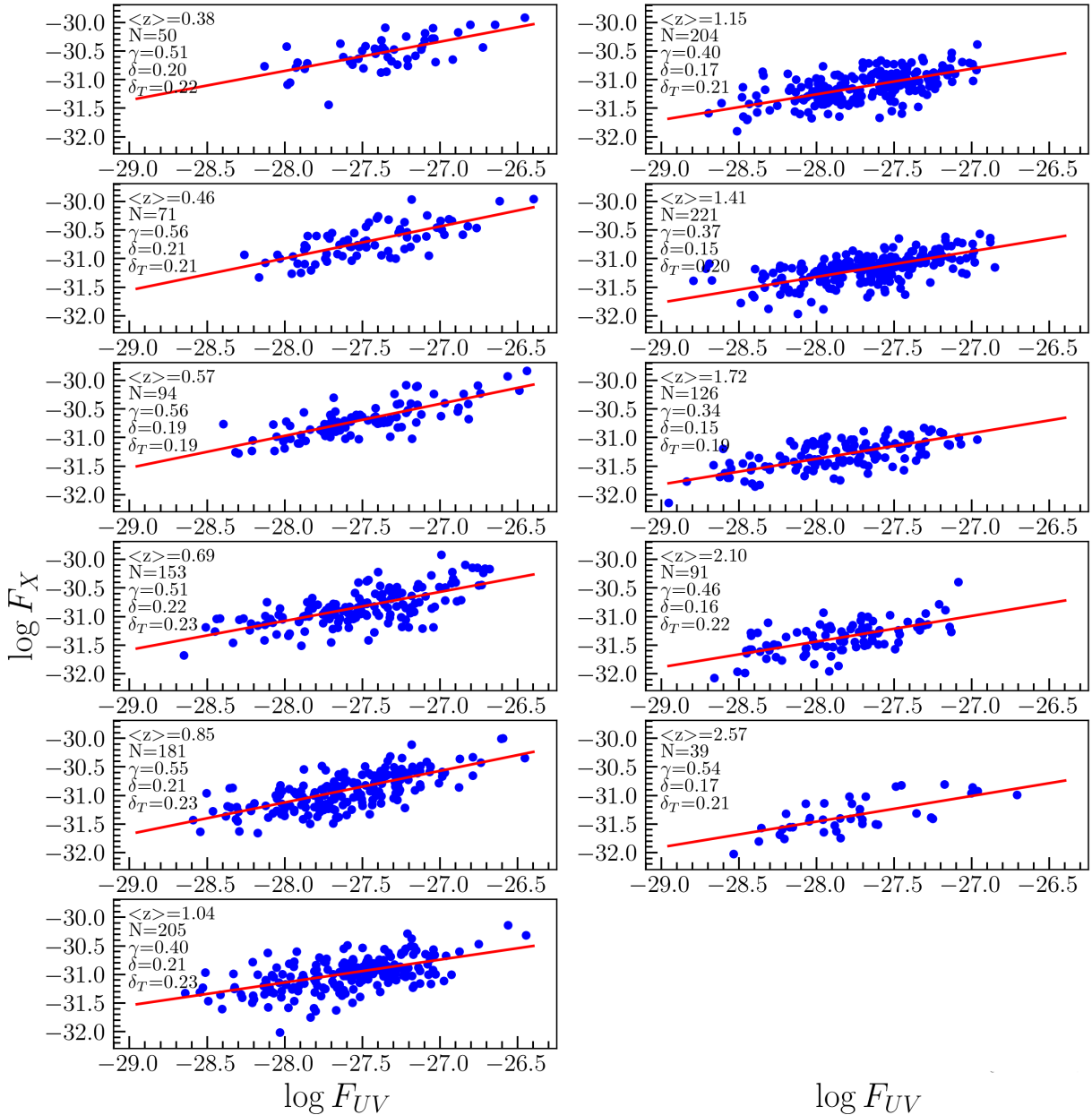


Fig. 5. f_X – f_{UV} relation in 11 redshift bins, obtained by using the 2500 Å monochromatic flux from the spectroscopic analysis as f_{UV} and the monochromatic flux at 1 keV as f_X . The best-fit parameters (slope and dispersion), the total dispersion, the number of objects, and the average redshift are also reported.

(i.e., with a wavelength shorter than 824.6 Å). Therefore, it is sensitive to the UV continuum blueward of the Lyman limit, which is not accessible through direct observations. Furthermore, its high equivalent width allows relatively precise flux measurements, and its rest-frame wavelength makes it observable in most of the redshift range of our spectroscopic sample. This combination of properties makes it the best candidate for our analysis, as it allows us to investigate whether the ~ 800 Å band is a more appropriate indicator of the disc emission than the 1350–5100 Å continuum. Alternative possibilities are the C IV $\lambda 1549$ Å line at higher redshifts (Lusso et al. 2021), or the H β $\lambda 4861$ Å line at lower redshift. The latter is indeed observable only up to $z \sim 0.8$.

The objects with spectra obtained with the SDSS spectrograph have Mg II emission up to a redshift of 2.28, while the ones

with spectra obtained with the BOSS spectrograph have Mg II emission up to a redshift of 2.71. However, the fitting procedure of the BOSS objects in the redshift range of $2.58 < z < 2.71$ returned a poor-quality flag for the Mg II line, suggesting that the line parameters are not reliably constrained when this is located at the extremity of the spectrum. We therefore restricted the analysis to the redshift range of $0.38 < z < 2.58$ using ten redshift bins. We obtain a mean value of the slope $\gamma = 0.60 \pm 0.02$, a mean dispersion parameter $\delta = 0.16$ dex, and a mean total dispersion $\delta_T = 0.19$ dex. We notice that the Mg II line flux as a UV flux indicator gives a higher value of the slope parameter when compared with the spectroscopically derived monochromatic flux at any tested optical–UV wavelength, yet the dispersion is significantly lower. In Fig. 6, we show the results of the fitting procedure using the Mg II line flux as f_{UV} for the ten redshift

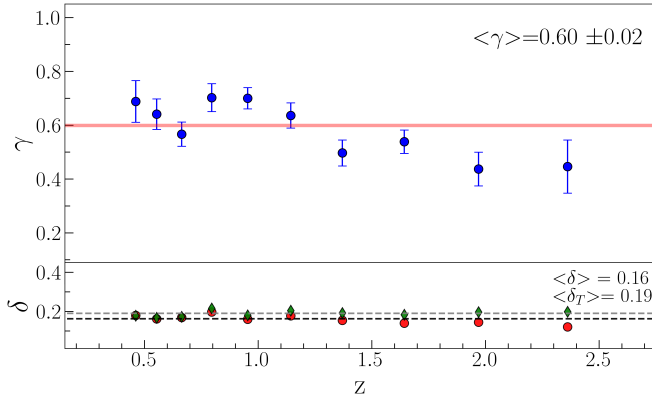


Fig. 6. Parameter γ as function of redshift, resulting from fit of Eq. (1) when Mg II emission line flux is used as f_{UV} and monochromatic flux at 1 keV is used as f_X . The mean value of γ is 0.60 ± 0.02 , and we can see that there is no clear trend with redshift.

bins. We checked the dependence of the γ parameter as a function of redshift with linear regression. The fit returns a γ - z relation with a slope of $m = -0.11 \pm 0.04$. Contrary to the previous two cases, there is evidence for a redshift trend, even if not a very strong one. We notice, however, that the analysis with the Mg II line is limited to a smaller maximum redshift, and the results in the common range are similar to those in Figs. 3 and 4 for the relations with the UV continuum. Another issue that might be affecting the Mg II results is the differences between objects with data coming from the SDSS spectrograph and the BOSS spectrograph. While we find no differences in the γ values and redshift dependence when comparing BOSS and SDSS data for the continuum, differences are found when comparing Mg II data. When fitting the f_X - f_{UV} relation with only SDSS objects, we find an average slope of $\gamma = 0.64 \pm 0.03$ and an even more significant redshift trend; thus, when fitting the slope γ as a function of redshift with a line, we find a slope coefficient of $m = -0.19 \pm 0.05$. When using only the BOSS data, instead, we find $\gamma = 0.61 \pm 0.03$ and no significant redshift trend, with $m = 0.08 \pm 0.06$.

4. Mg II line width as a possible additional parameter

The widths of emission lines are independent observables with respect to continuum or line fluxes, and they carry complementary information, such as the gas rotational velocity or its outflow velocity. These properties are in turn related to the physical parameters of the primary source (black hole mass, accretion rate, etc.). For this reason it is interesting to investigate whether the X-ray-to-UV relation is also dependent on line widths, as already extensively discussed in Lusso & Risaliti (2017). To perform this test, we employed the following modified relation in our fit:

$$\log(f_X) = \gamma \log(f_{UV}) + \eta \log(\text{FWHM}_{\text{Mg II}}) + \beta'', \quad (9)$$

where f_X is the monochromatic X-ray flux at 1 keV and $\text{FWHM}_{\text{Mg II}}$ is the FWHM of the Mg II emission line that we inferred with the UV spectral fitting procedure. The goals of this analysis are (a) to use possible additional correlations to decrease the intrinsic dispersion of the relation, and (b) to understand whether these correlations have an effect on the use of the X-ray-to-UV relation to estimate quasar distances. The analysis is carried out in the 0.38–2.58 redshift range, where the Mg II line is available, with ten bins.

When using the spectroscopically-derived monochromatic flux at 2500 Å as f_{UV} , we found a correlation which is highly significant, with a mean value of the parameter η equal to $\eta = 0.25 \pm 0.04$. The observed intrinsic dispersion is $\delta = 0.18$ dex and the total dispersion is $\delta_T = 0.20$ dex. We note that the δ and δ_T parameters that we obtain are comparable with the values presented in the previous section, where the dependence on the FWHM was not taken into account. It might be that the share of dispersion due to neglecting the FWHM correlation is too little for this effect to emerge and/or that the dynamical range of the FWHM values is too small for the additional correlation to impact significantly on the global observed dispersion. Regarding the parameter γ , we obtain a result consistent with the previous values, with $\gamma = 0.45 \pm 0.01$.

Using $f_{\text{Mg II}}$ as f_{UV} , instead, we found no correlation with the FWHM: we obtain $\eta = -0.03 \pm 0.03$, consistent with zero. This suggests that when $f_{\text{Mg II}}$ is employed most of the significance of the correlation between f_X and line properties is already embedded in the f_X - $f_{\text{Mg II}}$ relation, so also considering a dependence on the FWHM does not add any new information.

Given the high significance of the dependence of the X-ray flux on the FWHM parameter, the obvious next step of the analysis is to check for a possible correlation between the UV flux indicator and the FWHM. This correlation could in principle be relevant to the inversion of the X-ray-to-UV relation to obtain quasar distances and, in the worst case scenario, introduce some redshift-dependent bias. In order to perform this check, we needed to compute the covariance matrix for the fit of Eq. (9). However, given the small dynamical range of the quantity $\log(\text{FWHM})$ and the relatively small number of objects in each single redshift bin, we were not able to obtain significant estimates of the correlation between UV flux and FWHM in the redshift-resolved analysis. For this reason, we carried out the fitting procedure using luminosities instead of fluxes (derived with a standard flat Λ CDM cosmology) and considering the whole sample together, using the monochromatic 1-keV luminosity as L_X , the spectroscopically derived 2500 Å monochromatic flux as L_{UV} , and the FWHM of the Mg II line. We then derived and normalised with respect to the first term the covariance matrix of γ and η , and we diagonalised it, with the goal of finding the linear combination of L_{UV} and $\text{FWHM}_{\text{Mg II}}$ required to obtain variables that are independent of one another in our fitting procedure. We found the matrix of the eigenvectors to be

$$\begin{pmatrix} -0.999 & -0.045 \\ 0.045 & -0.999 \end{pmatrix},$$

which, multiplied by the variable column vector (L_{UV} , $\text{FWHM}_{\text{Mg II}}$), gives us the following new variables:

$$X = -0.999 L_{UV} - 0.045 \text{FWHM}_{\text{Mg II}} \quad (10)$$

$$Y = 0.045 L_{UV} - 0.999 \text{FWHM}_{\text{Mg II}}. \quad (11)$$

These new variables are independent of one another; if we repeat the described procedure using X, Y instead of L_{UV} , $\text{FWHM}_{\text{Mg II}}$ we find a diagonal covariance matrix.

This result also implies that we can implement a modified X-ray-to-UV flux-flux relation with the addition of the FWHM when this is available and keep using the standard relation otherwise. We performed this additional test in the whole redshift range of our sample, 0.38–3.48, again with 11 redshift bins, by modifying the likelihood accordingly. Using the photometric 2500 Å flux as f_{UV} and the 1 keV flux as f_X , we obtain $\gamma = 0.56 \pm 0.01$, $\delta = 0.16$ dex, $\delta_T = 0.19$ dex, $\eta = 0.25 \pm 0.04$.

Therefore, with this mixed likelihood, we have a slight decrease of both quantities on the black hole mass M_{BH} and the black hole accretion rate \dot{M}_{BH} . Said model predicts the slope between the X-ray luminosity (or flux) and the FWHM of the Mg II line to be $\hat{\eta} = 0.44^{+0.21}_{-0.19}$, and they found, for a sample of 545 quasars, an observed slope between the X-ray luminosity and the Mg II FWHM equal to $\eta_{\text{LR17}} = 0.54 \pm 0.07$, consistent with the toy model. Our result, $\eta = 0.25 \pm 0.04$, is also consistent with the prediction of the toy model. It significantly differs from the Lusso & Risaliti (2017) value, but we note that they performed the analysis (i) for the sample as a whole and not in redshift bins, using Λ CDM-derived luminosities, and (ii) using the photometric 2500 Å luminosity as L_{UV} instead of the spectroscopic one. If we perform the analysis in the same way, using the photometric luminosities for our sample, we obtain $\eta_{\text{phot}} = 0.45 \pm 0.04$, which is statistically consistent with the Lusso & Risaliti (2017) result.

However, our results do not entirely align with the toy model presented Lusso & Risaliti (2017). The model, indeed, implied also the presence of a L_{UV} –FWHM relation, while we find the two quantities to be uncorrelated. At the same time, it might be that the small dynamic range of the Mg II FWHM does not allow us to observe the correlation.

Since the observational dependence of the X-ray flux on the Mg II FWHM may be due to a physical dependence on the black hole mass, we performed an additional check by repeating our whole analysis for two subsamples with black hole mass estimates $M_{\text{BH}} < 10^{8.9} M_{\odot}$ and $M_{\text{BH}} < 10^{8.9} M_{\odot}$, respectively. We did not find any significant differences between these two subsamples. This suggests that the parameters of the relation do not directly depend on the black hole mass.

We finally have to consider that all the results that we have discussed in this subsection might be dependent on the cosmological model used to compute luminosities from fluxes. To test this possible dependence, we followed a cosmographic approach to fit the quasar Hubble diagram, as described in Bargiacchi et al. (2021). We found analogous results in terms of covariance matrices, eigenvectors and L_{UV} –FWHM dependence.

5. Discussion

The main results obtained through the various fits presented in the previous sections are the following.

First of all, the slope γ and the intrinsic dispersion δ of the X-ray-to-UV relation obtained by using spectroscopically derived 2500 Å fluxes are $\gamma \sim 0.46$ and $\delta \sim 0.22$ dex, respectively. Among the different proxies of the disc emission that we tested, the monochromatic flux at 2500 Å can be considered as the best available one, given its observational coverage over a broad redshift range. For the X-ray emission in the X-ray-to-UV relation, we find instead that the best monochromatic indicator (i.e., the one providing the smallest intrinsic dispersion) is the 1-keV flux.

When adopting the Mg II line flux as UV proxy, the obtained intrinsic dispersion is smaller than that obtained with monochromatic continuum fluxes ($\delta_{\text{Mg II}} \sim 0.17$ dex). The slope of the relation is instead significantly steeper ($\gamma_{\text{Mg II}} \sim 0.60$) than in the spectroscopic case. We also find that when the ‘photometric estimate’ of the UV monochromatic flux is adopted, the best-fit

parameters (both slope and dispersion) are consistent with those found using the Mg II line flux as UV proxy.

Finally, when the logarithm of the FWHM of the Mg II line is added to the relation, a statistically significant correlation is found, with a negligible decrease of the total intrinsic dispersion. The Mg II FWHM and UV flux parameters are not statistically correlated.

Here we discuss the interpretation and the main consequences of these results. The most remarkable result of our analysis is arguably that the spectroscopically derived 2500 Å monochromatic flux delivered a significantly lower γ value when used as f_{UV} compared to the Mg II line flux. This trend can be explained as a consequence of the non-linear relation between the emission-line equivalent width (EW) and the luminosity of the quasar continuum, known as the Baldwin effect (Baldwin 1977). We analysed the relation between the Mg II luminosity and the monochromatic luminosity at 2500 Å derived from the spectroscopic analysis of our sample and we obtained a slope of ~ 0.8 . In order to fit the whole sample simultaneously, for this analysis we used luminosities instead of fluxes, assuming a standard flat Λ CDM model with $\Omega_{\text{M}} = 0.3$ and $H_0 = 70 \text{ km s}^{-1} \text{ Mpc}^{-1}$. We checked that the results are not significantly dependent on the choice of the cosmological model.

If we now consider the relation between the X-ray and UV luminosities as $\log(L_{2\text{keV}}) = \gamma \log(L_{2500}) + \beta$, with $\gamma = 0.46$ as shown in Sect. 2, and we use the $\log(L_{2500}) - \log(L_{\text{Mg II}})$ mentioned above, we obtain a slope of the $\log(L_{2\text{keV}}) - \log(L_{\text{Mg II}})$ of $0.46/0.8 = 0.58$, which is fully consistent with the slope of the relation that we obtain when using the Mg II luminosity (or flux) as L_{UV} , as shown in Sect. 4. Therefore, we conclude that the reason behind different X-ray to UV relations when shifting from continuum UV proxies to line proxies is associated with the presence of the Baldwin effect itself.

Another result related to the adoption of the Mg II as UV proxy is the smaller intrinsic dispersion δ of the X-ray to UV relation with respect to the monochromatic continuum indicators. Considering that this line requires an ionising continuum at wavelengths shorter than 824 Å, a possible interpretation of this result is that an even tighter relation must exist between the X-ray flux and the UV flux blueward of the Ly limit. In this scenario, the monochromatic fluxes at optical or near-UV wavelengths are all ‘secondary indicators’ with a similar relation to the primary one.

The slope parameter that we obtain when using the ‘photometric’ UV flux has a less obvious interpretation. The photometric flux is a complex UV proxy, as it contains contributions from both the quasar continuum and line emissions. Moreover, even if it is formally a monochromatic quantity, it is derived from the wide-band photometric fluxes. We notice that its value is similar to the one obtained using the Mg II line as a UV proxy and that the dispersion of the relation is marginally better than the one obtained with truly monochromatic fluxes. This suggests that the combined information used to derive the photometric flux is similar to that contained in the Mg II flux, and is more closely related to the UV emission at $\lambda \sim 800$ Å than the monochromatic fluxes.

In Fig. 7, we show the relation between the luminosity of the Mg II line and the photometric luminosity at 2500 Å. The slope is statistically consistent with unity, which explains the similar behaviour of these two quantities when used as f_{UV} proxies in the X-ray-to-UV relation.

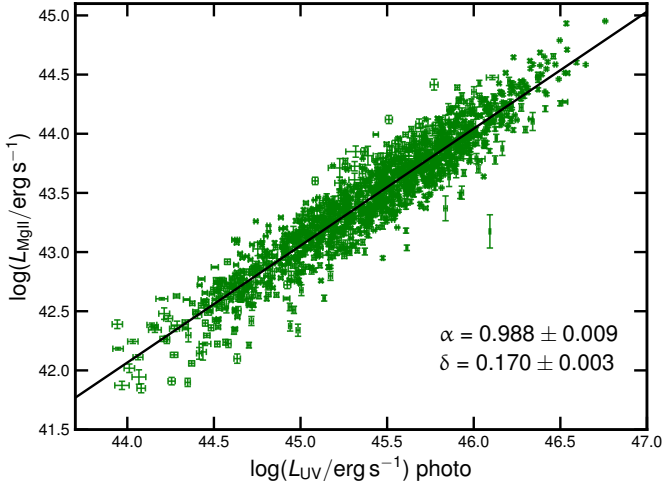


Fig. 7. Relation between the luminosity of the Mg II line and the luminosity at 2500 Å derived from photometry.

6. Cosmological application

The most relevant result of our analysis concerning the use of quasars as standard candles through the X-ray-to-UV relation is the confirmation of such relation with spectroscopic data. Since there are no known standard candles at redshifts higher than ~ 1.5 , it is impossible to have an ‘external’ test of the validity of the relation in a cosmology-independent way. The only way to confirm or falsify the method is through an analysis of the possible redshift dependent physical and/or selection effects that may bias the distance estimate. In this sense, the complete UV (rest-frame) spectral analysis is a significant step forward; possible biases related to the use of the optical broad-band magnitudes (e.g., due to dust reddening or to the effect of strong lines moving into or out of the photometric bands depending on the redshift) are ruled out, and the flux measurements are directly done from the spectral fits.

The second fundamental outcome of our work is the first systematic search of the best X-ray and UV proxies of the relation, within the spectral range covered by the available spectroscopic data. While the best X-ray and UV indicators turned out to be the monochromatic flux at 1 keV and the Mg II flux, respectively, we found that the intrinsic dispersion of the relation with the other proxies is only slightly larger. In particular, the ‘standard’ indicators, which are the monochromatic flux at 2500 Å derived from the photometric data and the monochromatic flux at 2 keV, are almost as effective as the ‘best’ ones.

This result suggests that none of the indicators used here is the primary driver of the relation. In order to prove this statement, we can consider our best UV indicator, that is the Mg II flux and the intrinsic dispersion of the X-ray–UV relation, $\delta_{\text{Mg II}}$, obtained with this indicator. If the Mg II flux were the primary driver of the relation (i.e., the physical relation involves either the Mg II flux or a tightly related quantity), we would expect that the dispersion δ of the X-ray-to-UV relation using another UV proxy would be related to $\delta_{\text{Mg II}}$ through the following relation: $\delta^2 = \delta_{\text{Mg II}}^2 + \Delta^2$, where Δ is the dispersion of the relation between the Mg II flux and the other UV indicator. However, this is not the case; for example, the dispersion of the relation between the Mg II flux and the monochromatic flux at 2500 Å is $\Delta = 0.15$ dex, which would imply $\delta \sim 0.25$ dex, while the observed value is $\delta = 0.19 \pm 0.01$ dex (see Fig. 6). We conclude that both the UV indicators used here are proxies of a more fun-

damental one, probably related to the UV emission blueward of the Lyman limit.

A final result with some implications for the use of quasars as standard candles is the relation between the X-ray and UV fluxes and the FWHM of the Mg II emission line. We tested the inclusion of this parameter in the X-ray-to-UV flux relation, using the photometric 2500 Å flux as f_{UV} . Just like in the spectroscopic case, we found that there is no correlation between the UV flux and the Mg II FWHM. Therefore, we can incorporate an additional term in the relation between fluxes when the FWHM of the Mg II emission line is available, while fitting the ‘traditional’ relation if not. When doing so, we obtain $\gamma = 0.58 \pm 0.01$, $\delta = 0.16$ dex, and $\delta_{\text{T}} = 0.19$ dex.

We applied the results discussed above to the construction of a new Hubble diagram of quasars, based on the spectroscopic quasar sample described in this work. We derived the luminosity distances using Eq. (9) for objects for which the Mg II line is available, and the standard relation for those for which it is not. We used the 1-keV monochromatic flux as f_{X} . As for f_{UV} , we used both the spectroscopic and the photometric monochromatic flux at 2500 Å (we also repeated the computation using the Mg II flux, obtaining fully consistent results). The results are shown in Fig. 8, where we also plot the supernovae of the Pantheon sample (Scolnic et al. 2018), used for the absolute calibration. Petrosian et al. (2022) argued that the analysis in redshift intervals may bias the cosmological analysis. We stress that we never considered any binning (especially when considering redshifts) to perform the cosmological analysis in our previous works. The same consideration can be applied here as well. The distance modulus of each individual quasar is obtained from Eqs. (9) and (10), and the fits of the Hubble diagram are done by marginalising over the parameters γ and β of the relation. As a consequence, the red points shown in Fig. 8 are computed only after the best fit values of these parameters are obtained, and they are shown only for illustrative purposes.

The Hubble diagram in Fig. 8 is relevant for two main reasons. First, the two versions of the diagram, with the two different methods to derive the UV monochromatic flux, are in full agreement. This was not granted a priori; if some systematic effect related to the derivation of the photometric fluxes were present, it would have been revealed by the comparison with the spectroscopy-based values. The photometric fluxes are much easier to obtain, and indeed we always used these values in our previous works. Therefore, this result is also a validation of the Hubble diagrams in Risaliti & Lusso (2019) and Lusso et al. (2020), which revealed a strong tension with the ‘concordance’ flat Λ CDM model.

Second, the dispersion in the Hubble diagram based on spectroscopic points is significantly lower than that based on photometric fluxes. This is the consequence of the different slopes of the X-ray-to-UV relation depending on which UV flux is used: $\gamma_{\text{phot}} \sim 0.6$ for the photometric fluxes and $\gamma_{\text{spec}} \sim 0.45$ for the spectroscopic ones. Considering the error propagation from the relation to the distance moduli plotted in Fig. 8, the main contribution to the error is the intrinsic dispersion of the relation, divided by a factor $(1 - \gamma)$. This term implies that the uncertainty on the distances derived from spectroscopic fluxes is lower than that of distances based on photometric fluxes by a factor of $(1 - \gamma_{\text{phot}})/(1 - \gamma_{\text{spec}}) \sim 0.75$.

The tension with the standard flat Λ CDM model of the spectroscopic sample discussed in this paper has a statistical significance of 3σ . This is lower than previously published results based on larger samples (Lusso et al. 2020; Bargiacchi et al. 2021)

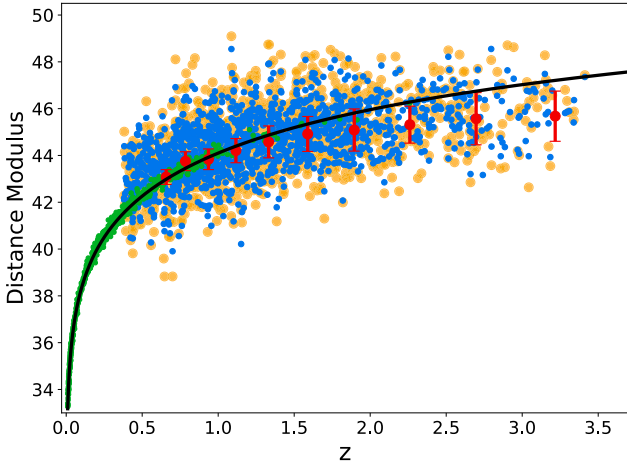


Fig. 8. Hubble diagram of supernovae and quasars. Green points are supernovae Ia from the Pantheon sample (Scolnic et al. 2018), yellow points are quasars with distances derived using the photometric UV fluxes, blue points are quasars with distances derived using the spectroscopic UV fluxes, and red points are the average distance modulus values for spectroscopic quasars in the individual redshift bins. The normalisation parameter for quasars is chosen in order to match that of supernovae Ia. As in our previous studies (Risaliti & Lusso 2019), we do so by cross-matching the Hubble diagram of quasars with that of supernovae in the common redshift range. The black line represents the prediction of a flat Λ CDM model with $\Omega_M = 0.3$.

but, again, it is the first result based on a sample with complete control on the derivation of the UV fluxes.

7. Summary and conclusions

In this paper, we present a thorough UV spectral analysis of 1764 quasars from the Lusso et al. (2020) sample with the main aims being to discuss the choice of the L_X and L_{UV} indicators and to establish whether it is possible to further reduce the observed dispersion to gain a better understanding of the physics behind the L_X-L_{UV} relation. We thus derived monochromatic luminosities at five different wavelengths as well as the emission-line properties. We compared our results with the spectral analysis of Wu & Shen (2022) and we found a good agreement (see Appendix A). We also computed the X-ray properties of our sample from a spectroscopic analysis for objects at a redshift higher than 1.9, while we used photometric data for objects at lower redshift (see Appendix B). Our main results are summarised below.

1. We obtained the monochromatic flux at 2500 \AA from a detailed spectroscopic analysis, as this is supposed to be a more accurate measurement than the one derived from the photometric data. We then analysed the L_X-L_{UV} relation in narrow redshift bins so that we could (i) use fluxes instead of luminosities and therefore be independent of any chosen cosmology, and (ii) look for possible redshift trends of the slope parameter γ . While the slope is confirmed not to show any systematic trend with redshift, its value of $\gamma \sim 0.46$ is lower (flatter) than those found in our previous studies where photometric data were used. Also, the dispersion parameter δ is slightly higher when using spectroscopically derived monochromatic fluxes as f_{UV} . If the true physical quantity behind the L_X-L_{UV} relation had been the monochromatic luminosity at 2500 \AA (or any of the wavelengths that we tested; see below) we would have expected better results in
2. We investigated what the best energies to be used as L_X and L_{UV} are, following the assumption that both the UV and the X-ray continua of quasars can be parameterised as power laws and studying the dependence of the X-ray-to-UV relation on the respective spectral slopes. We stress that we do not expect the relation to subsist between two monochromatic luminosities, but we are looking for the best possible proxies for the overall UV (disc) and X-ray (corona) emission. In the X-rays, we find that there is a preference for 1 keV as the characteristic energy, as it is the one less sensitive to the actual spectral slope. When using the 1-keV fluxes instead of the 2-keV ones, we indeed found a lower dispersion. Unfortunately, given the redshift range of our sample, the 1-keV flux is on average measured with higher uncertainties than the 2-keV ones. This partly undermines the advantage of having found the characteristic energy because the resulting total dispersion is only slightly lower. Still, the fact that the total dispersion decreases even if we are using a ‘worse’ proxy in terms of uncertainties means that physically the relation is indeed tighter when we are using the 1-keV flux as f_X . In the UV, we find no conclusive indications on a specific characteristic wavelength. This might be explained if the ‘true’ physical quantity is found at much shorter wavelengths, beyond the peak of the disc emission, so assuming the optical-UV power law is less appropriate and/or informative. Consequently, we argue that the best choice is the 2500 \AA flux simply because it is the one that results in a marginally lower dispersion. This might be because this wavelength falls in the observed spectra for the wider redshift range in our sample, implying a lower number of objects for which fluxes are determined via extrapolation and therefore with larger uncertainties.
3. When using the integrated Mg II line flux as f_{UV} , we obtain a higher (steeper) slope value ($\gamma \sim 0.6$) and a lower dispersion ($\delta = 0.16 \text{ dex}$) compared to any other UV continuum indicator derived from the spectroscopic analysis. We note that although the Mg II emission line is found at 2800 \AA , its flux strongly depends on the quasar emission at much shorter wavelengths, around $\sim 800 \text{ \AA}$. Therefore, it might be that the physical relation behind the X-ray and UV luminosities is more strongly linked to the quasar emission at shorter wavelengths, and that as a consequence the Mg II emission-line flux works as a better proxy when compared to the fluxes in the $1350-5500 \text{ \AA}$ range. Unfortunately, the Mg II emission line is only available for the objects in our sample up to $z \sim 2.5$. Another possible explanation is that when we consider an indicator such as the Mg II emission line, which strongly depends on the extreme-UV SED shape, a tighter correlation with the soft X-ray can naturally arise due to the energy proximity of the bands involved.
4. The comparison between the values of the slopes that we found when using, respectively, the Mg II line fluxes and the spectroscopic monochromatic fluxes, is entirely consistent with the presence of the Baldwin effect.
5. We confirm a correlation between the X-ray and UV flux taking into account the FWHM of the Mg II line, while the UV flux and the FWHM turn out to be not significantly

correlated. This non-correlation allows us to include the FWHM in the X-ray/UV flux relation whenever available, and to keep using the standard relation otherwise. In this way, we can overcome the redshift limitations on the Mg II flux and still obtain a lower dispersion for the whole sample.

6. The Hubble diagram obtained from spectroscopic UV data is fully consistent with that obtained with photometric data. This is a validation of the previous results based on ‘photometric’ Hubble diagrams. Moreover, the ‘spectroscopic’ Hubble diagram shows a tension at statistical level of $\sim 3\sigma$ with the flat Λ CDM model. In previous works (e.g., Lusso et al. 2020; Bargiacchi et al. 2021), we obtained a higher significance of this tension, thanks to a wider redshift extent than the sample considered here. However, the Hubble diagram presented here is the first one where we have fully checked the UV spectral properties of the sources (and also the X-ray ones at $z > 1.9$).

Overall, the results presented in this work are another step towards the validation of the non-linear X-ray-to-UV relation of quasars as a reliable distance indicator. Since a limited number of supernovae Ia are available at redshifts higher than ~ 1.5 and, by construction, a cosmology-independent validation of the method is impossible, the only way to further check our method is to search for possible evolutionary effects in the spectral emission of the quasars included in our Hubble diagram. In Sacchi et al. (2022), we demonstrated that the average continuum and line properties of quasars at $z > 2.5$ are perfectly matched to the ones of lower redshift counterparts in both the UV and X-rays. An extensive analysis of the stacked SDSS spectra in bins of BH mass and Eddington ratio for all the sources of the current sample is currently ongoing (Trefoloni et al., in prep.). We expect that future observations of supernovae at $z > 1.5$ will be able to independently probe any deviation from the concordance model found with the Hubble diagram of quasars.

Acknowledgements. We thank the referee for their detailed and constructive suggestions. We acknowledge financial contribution from the agreement ASI-INAF n.2017-14-H.O. EL acknowledges the support of grant ID: 45780 Fondazione Cassa di Risparmio Firenze.

References

- Arnaud, K. A. 1996, in *Astronomical Data Analysis Software and Systems V*, eds. G. H. Jacoby, & J. Barnes, *ASP Conf. Ser.*, 101, 17
- Baldwin, J. A. 1977, *ApJ*, 214, 679
- Bargiacchi, G., Risaliti, G., Benetti, M., et al. 2021, *A&A*, 649, A65
- Bargiacchi, G., Benetti, M., Capozziello, S., et al. 2022, *MNRAS*, 515, 1795
- Calderone, G., Nicastro, L., Ghisellini, G., et al. 2017, *MNRAS*, 472, 4051
- Elvis, M., Hao, H., Civano, F., et al. 2012, *ApJ*, 759, 6
- Foreman-Mackey, D., Hogg, D. W., Lang, D., & Goodman, J. 2013, *PASP*, 125, 306
- Haardt, F., & Maraschi, L. 1991, *ApJ*, 380, L51
- Haardt, F., & Maraschi, L. 1993, *ApJ*, 413, 507
- Khadka, N., & Ratra, B. 2021, *MNRAS*, 502, 6140
- Krolik, J. H., & Kallman, T. R. 1988, *ApJ*, 324, 714
- Lusso, E., & Risaliti, G. 2016, *ApJ*, 819, 154
- Lusso, E., & Risaliti, G. 2017, *A&A*, 602, A79
- Lusso, E., Comastri, A., Vignali, C., et al. 2010, *A&A*, 512, A34
- Lusso, E., Risaliti, G., Nardini, E., et al. 2020, *A&A*, 642, A150
- Lusso, E., Nardini, E., Bisogni, S., et al. 2021, *A&A*, 653, A158
- Meyer, F., Liu, B. F., & Meyer-Hofmeister, E. 2000, *A&A*, 361, 175
- Netzer, H. 1980, *ApJ*, 236, 406
- Petrosian, V., Singal, J., & Mutchnick, S. 2022, *ApJ*, 935, L19
- Rakshit, S., Stalin, C. S., & Kotilainen, J. 2020, *ApJS*, 249, 17
- Richards, G. T., Lacy, M., Storrie-Lombardi, L. J., et al. 2006, *ApJS*, 166, 470
- Risaliti, G., & Lusso, E. 2019, *Nat. Astron.*, 3, 272
- Sacchi, A., Risaliti, G., Signorini, M., et al. 2022, *A&A*, 663, L7
- Sanders, D. B., Phinney, E. S., Neugebauer, G., Soifer, B. T., & Matthews, K. 1989, *ApJ*, 347, 29
- Scolnic, D. M., Jones, D. O., Rest, A., et al. 2018, *ApJ*, 859, 101
- Scolnic, D., Brout, D., Carr, A., et al. 2022, *ApJ*, 938, 113
- Shakura, N. I., & Sunyaev, R. A. 1973, *A&A*, 24, 337
- Steffen, A. T., Strateva, I., Brandt, W. N., et al. 2006, *AJ*, 131, 2826
- Svensson, R. 1982, *ApJ*, 258, 321
- Svensson, R., & Zdziarski, A. A. 1994, *ApJ*, 436, 599
- Tananbaum, H., Avni, Y., Branduardi, G., et al. 1979, *ApJ*, 234, L9
- Wu, Q., & Shen, Y. 2022, *ApJS*, 263, 82
- Young, M., Elvis, M., & Risaliti, G. 2010, *ApJ*, 708, 1388

Appendix A: UV spectral analysis

We performed the fit of the SDSS UV spectra for the 1764 objects in our sample with the IDL package QSF_{it} (Calderone et al. (2017)). This software allowed us to fit the AGN continuum, the Balmer continuum, the emission-line and iron-complex properties, and the host-galaxy component. Regarding the host galaxy, a single template of an elliptical galaxy was used to determine its contribution to the total luminosity. The code is highly customizable, and our main settings are as follows: for quasars with redshifts below 0.6, given that the host-galaxy luminosity can be a relevant share of the total luminosity, the slope of the quasar continuum is degenerate with the host galaxy normalisation. Therefore, there is no way to determine it in a reliable way. We consequently fixed the value of the continuum slope for such quasars as $f_{\lambda} \propto \lambda^{-1.7}$. Each emission line was fitted with a Gaussian profile. QSF_{it} allowed us to consider both a broad and narrow component to fit each line and to add unknown components if necessary. In case the code is not able to correctly disentangle the broad and the narrow component of the main emission lines, we used a composite profile of a broad component and an unknown one to account for the residuals. With this method, what we obtained are the *total* emission line properties, rather than the separated properties of broad and narrow components. Full width at half maximum (FWHM) upper limits were set to 2000 km/s for unknown and narrow lines and to 10,000 km/s for broad lines. To avoid fitting regions of the spectrum contaminated by intergalactic absorption, the minimum wavelength for model fitting was set to 1450 Å (rest frame) for all the objects in our sample.

The strength of the QSF_{it} code is that the spectral properties are all fitted simultaneously. This way, one can reasonably assume that the obtained continuum properties do not depend on local features of the spectrum itself.

At the end of the fitting procedure, for each quasar we obtained the continuum slope and the monochromatic luminosity at 2500 Å. We also recorded the luminosity values at 1350 Å, 3000 Å, 4400 Å, 5100 Å. If one or more of these wavelengths was out of the spectral range for a given spectrum, we extrapolated its value adopting the best-fit continuum slope. In terms of line properties, we obtained total flux, FWHM, offset velocity, and equivalent width. Together with the line properties and their errors, quality flags for each line were given. Regarding the quality flag, the QSF_{it} code automatically raises a flag whenever one or more of the following situations occur: (i) the value of the continuum luminosity, a line's FWHM, or its offset velocity is NaN or equal to zero; (ii) any of the previous quantities hits a boundary value in the fit; (iii) the relative uncertainty on the continuum luminosity is higher than 1.5; (iv) the relative uncertainty on the FWHM of a given line is higher than 2; (v) the uncertainty on the velocity offset is higher than 500 km s⁻¹. Objects with bad-quality flags were removed from the sample.

After the fitting procedure, each spectrum was visually inspected and a second quality flag was raised if (i) the residuals of the fitting procedure showed a systematic trend as a function of wavelength or (ii) the mean reduced χ^2 value was higher than 2. Since in these cases the monochromatic luminosities estimates could not be considered reliable, such sources were removed from the sample. As a consequence, our sample size decreased from 1764 to 1705 sources. Among them, 1217 also have good Mg II emission line properties (line luminosity, FWHM, EW, velocity offset), while 403 have H β , 305 have [O III] λ 4959Å, 291 have [O III] λ 5007Å (202 have both the doublet components), 493 have C IV. In Figure A.1 we show, as an example, the spectra of four objects at different redshifts and the best-fit results of the QSF_{it} analysis.

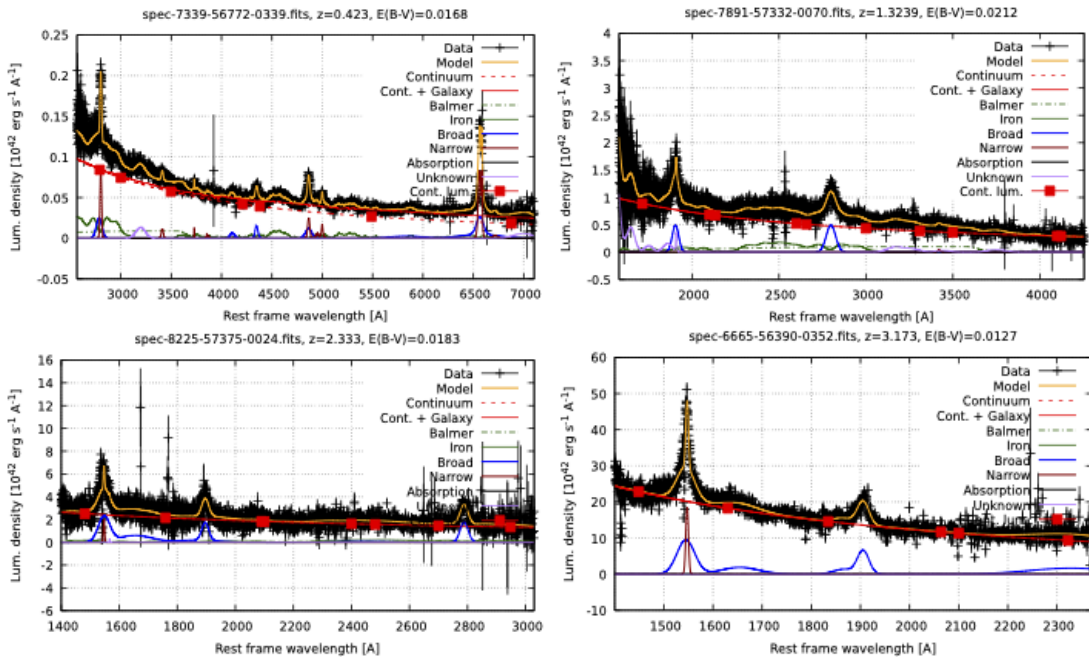


Fig. A.1. Four spectra at different redshifts and QSF_{it} best-fit results, in yellow. The different components are shown in the legend on the right of each panel.

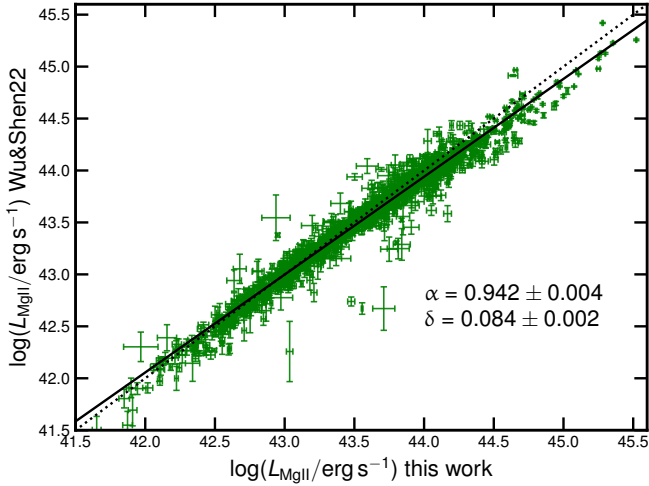


Fig. A.2. Comparison between the Mg II luminosity as derived from Wu & Shen (2022) and the Mg II luminosity derived in this work, in logarithmic units (erg s^{-1}). The dotted line is the one-to-one relation. We also report the best-fit slope and dispersion and the resulting best-fit regression line as the solid black line.

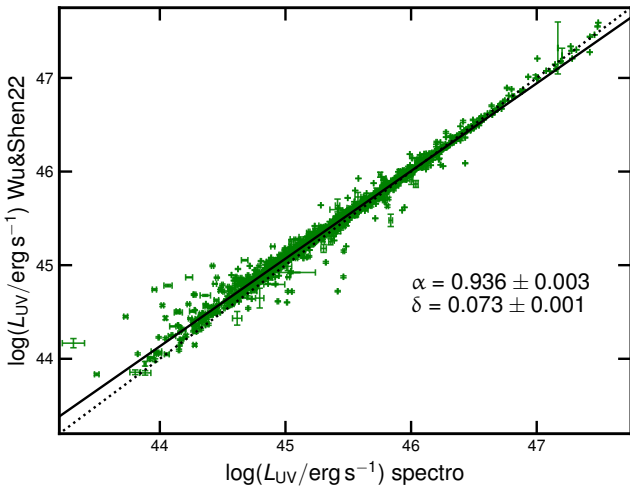


Fig. A.3. Comparison between monochromatic luminosity at 2500 Å obtained from our spectral analysis and the one from the Wu & Shen (2022), in logarithmic units (erg s^{-1}). The dotted line is the one-to-one relation. We also report the best-fit slope and dispersion and the resulting best-fit regression line with the solid black line. There is an overall good agreement between the two measurements.

In Figure A.2, we compare our estimates of the total luminosity of the Mg II line with the one derived from the Wu & Shen (2022) catalogue. We can see an overall good agreement. Comparisons between other emission line properties show similar results. We also performed the same comparisons with the results of Rakshit et al. (2020), and they gave analogous results.

Wu & Shen (2022) presented the detailed measurements of the spectral properties of $\sim 500,000$ quasars from the latest release of the Sloan Digital Sky Survey (SDSS-DR16) quasar catalogue, which were used to validate the results of our spectral analysis. Regarding the monochromatic luminosities, we find a very good match, as can be seen in Figure A.3 for the monochromatic luminosity at 3000 Å. We can also see that the match is excellent at high luminosities, while some scatter is present for less luminous objects. This mainly depends on the different

host-galaxy fitting techniques that have been employed; we used a single host-galaxy template, while in Wu & Shen (2022) the galaxy is not characterised. Quasars with lower luminosities are also the ones more affected by the host-galaxy contribution, so we expect higher discrepancies for such objects. Comparisons with the other monochromatic luminosities at different wavelengths (1350 Å, 4400 Å, 5100 Å) all show analogous results.

Appendix B: X-ray spectral analysis

All the objects in our sample have an estimate of the rest-frame 2-keV monochromatic flux derived from *XMM-Newton* photometric data. A detailed description of the procedure can be found in Section 4 of Lusso et al. (2020).

We have performed a full spectroscopic analysis for a subsample of 292 objects, which are all the objects in our sample at redshifts higher than 1.9, for which any discrepancy between the photometric and spectroscopic values can have major consequences in terms of cosmological applications. This comes as an extension of the X-ray spectroscopic analysis provided in Sacchi et al. (2022) for objects at redshifts higher than 2.5.

The goal of this analysis is to prove that not using fully spectroscopic X-ray fluxes does not introduce any bias in our results, while showing that part of the residual observed dispersion of the $L_X - L_{UV}$ relation can be attributed to the lower accuracy of photometric measurements at the same time. We followed the standard procedure from the *XMM-Newton* user manual to obtain the spectra. For each object, we extracted three spectra for the three *XMM-Newton* cameras (pn, MOS1, and MOS2). We then combined the two MOS spectra into a single one.

The fit procedure was performed with the package XSPEC version 12.12 (Arnaud 1996). We subtracted the background from the spectrum and then fitted it with a power-law model, considering Galactic photoelectric absorption. We fitted the pn and the MOS spectra simultaneously, imposing the same spectral shape and allowing for a varying normalisation constant between the two cameras. From the best fit, we estimated the monochromatic flux at 1 keV, the monochromatic flux at 2 keV, and the photon index Γ , together with their 1σ uncertainties. In Figure B.1 we show, as an example, the spectra and the best-fit model for three objects, with data of different quality and therefore different uncertainties on the determination of the monochromatic X-ray flux at 2 keV. In Figure B.2, we show the comparison between the monochromatic fluxes at 2 keV derived from this spectroscopic analysis with the ones obtained with the standard procedure. The relation between the two quantities was fitted with a linear relation, and the best fit is statistically consistent with a one-to-one relation, with the linear regression returning a slope of $m = 1.01 \pm 0.01$ as the best fit. In Figure B.3, we also show the histogram of the differences between the spectroscopic and the monochromatic 2 keV fluxes, expressed in units of the standard deviation σ . We also see from this distribution that there is no systematic shift between the two quantities. Neither is there a significant skewness of the distribution, the skewness parameter being $k = 0.27 \pm 0.30$.

From this comparison, we infer that by using the spectroscopic data only for a subsample of objects we are not introducing any systematics. At the same time, there is a significant scatter between the spectroscopic and the photometric flux estimates. We can assume that the spectroscopic analysis is the more accurate one. This means that for those objects for which we are (still) using photometric data, we are actually introducing a contribution to the total observed dispersion when fitting the $L_X - L_{UV}$ relation. We should also note that from the complete

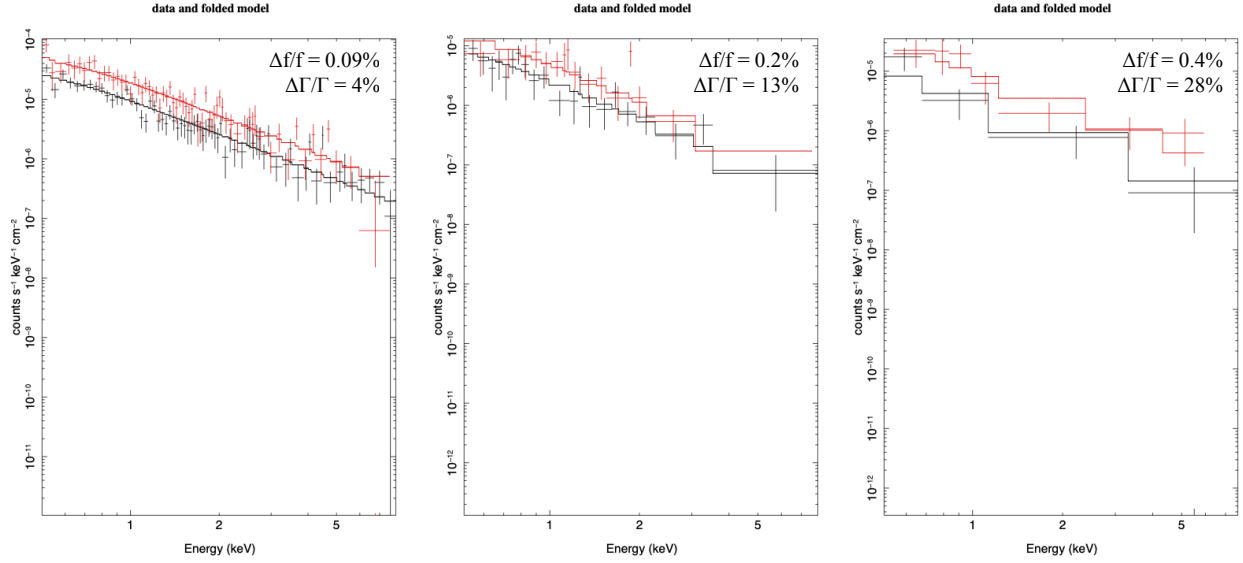


Fig. B.1. Example of X-ray spectrum and best fit of three sources at redshift 2.138, 2.144, 2.293. The pn spectrum is shown in red, and the MOS spectrum is shown in black. The relative uncertainties on the free parameters (the monochromatic flux at 2 keV and the photon index Γ) are shown as well.

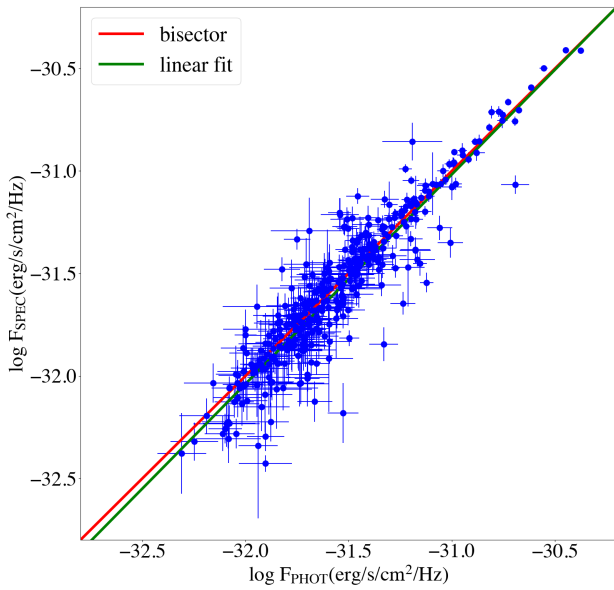


Fig. B.2. Comparison between photometrically derived 2-keV monochromatic fluxes and spectroscopically derived ones. The red line represents the one-to-one relation, while the green line is the best fit of the relation between the two quantities.

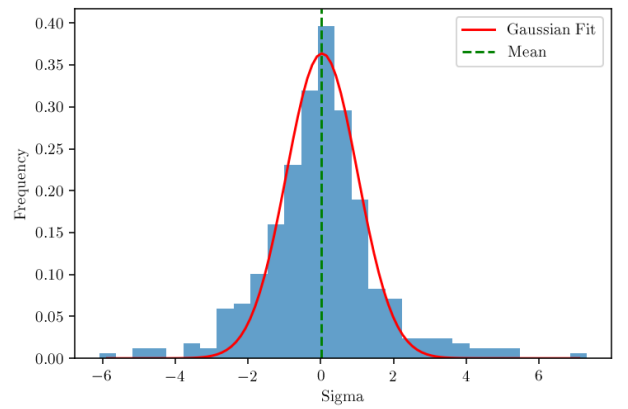


Fig. B.3. Histogram of differences between photometric and spectroscopic X-ray fluxes at 2 keV, shown in units of standard deviations. The red line shows the results of a Gaussian fit, which shows that the distribution is centred around zero. There is no significant skewness, as the skewness parameter turns out to be $k = 0.27 \pm 0.30$. This shows that there is no systematic shift between the two quantities.

X-ray spectroscopic analysis we are also able to check one by one that the observations are not affected by any bias, which is a possible cause of additional dispersion. A discussion of the contribution of X-ray observational issues to the total observed dispersion of the $L_X - L_{UV}$ relation will be addressed in a forthcoming paper. Analogous results in terms of the comparison between photometric and spectroscopic data are found when comparing the 1-keV monochromatic fluxes.